Supplementary Information

Scaling behavior in steady-state contracting actomyosin networks

Maya Malik-Garbi, Niv Ierushalmi, Silvia Jansen, Enas Abu-Shah, Bruce L. Goode, Alex Mogilner and Kinneret Keren

Supplementary Text

Viscoelastic contribution is dominated by the viscous stress

Generally, cellular actin networks are viscoelastic, with complex mechanical properties that can be approximated by a combination of Maxwell and Kelvin-Voight models [1-5]. These cited studies show that if a continuous stress is applied to an actin network, there is a short-term elastic response followed by a long-term viscous, flow-like behavior. The viscoelastic relaxation time – the time after which the elastic response fades and the viscous behavior ensues – was measured to be as short as a few seconds [3-5] (or even ~ 0.1 second [1]), much shorter than the characteristic timescales of actin network turnover and contraction, ~ 1 minute, in our system. Moreover, the elastic part of the viscoelastic stress and non-Newtonian components of the stress in the actin networks on long time scales were shown to be less than 10% of the total stress [6]. Therefore, we model the actin network as a purely viscous fluid.

Friction between the fluid and actin network is negligible

The Darcy friction forces between the porous polymer mesh and the fluid squeezing through it can be estimated as the characteristic actin network flow rate, ~ 0.1 μm/s, divided by the hydraulic permeability of the cytoskeleton, ~ 0.01 $\mu m^3/(pN\times s)$ [7], so the order of magnitude of the respective stress is ~ 10 $pN/\mu m^2$. The characteristic myosin contractile stress is usually on the order of ~ 100 $pN/\mu m^2$ [8, 9]. Measurements of the characteristic viscoelastic network stress that balances the myosin contractile stress also gave estimates of ~ 100 $pN/\mu m^2$ [10]. Thus, the Darcy friction forces between the actin mesh and the fluid squeezing through it are an order magnitude smaller than the myosin contractile stress and the viscoelastic network stress, and hence can be neglected.

Estimates of myosin-generated stress and actin network viscosity

We base our estimates of the myosin-generated contractile stress and of the actin network viscosity on measurements of the concentration of actin and myosin in *Xenopus* extract which are on the orders of 20 µM and 1 µM, respectively [11]. Such myosin concentration corresponds to ~ 600 myosin molecules in one cubic micron. Assuming that the average actin filament length is on the order of 0.1 µm, and the size of a myosin molecule is on the order of 0.1 µm, ~ 60 myosin molecules act per one layer of actin network 0.1 µm thick with a base area of 1 μm^2. Each myosin molecule generates ~ 1 pN force, and so we estimate the myosin-generated contractile stress as σ_A ~ 60 $pN/\mu m^2$ (this is in agreement with the characteristic measured myosin contractile stress [8, 9] which is typically on the order of ~ 100 $pN/\mu m^2$). The actin concentration in cells is, in fact, also on the order of tens of µM (away from very dense actin networks, such as lamellipodia and filopodia). Thus, we can estimate the network viscosity from viscosity measurements in low-density network regions in live cells which give values on the order of, μ~ 2×10^3 Pa×s [1]. According to our model, this leads to a contraction rate equal to $k \sim \sigma_A/\mu \sim 0.03\ s^{-1}$. This is in a good agreement with our measurement of $k \sim 1\min^{-1} \sim 0.02\ s^{-1}$.

Network contraction with an excluded region

We consider a spherically-symmetric network with a radial flow velocity field $V(r)$ and an inner exclusion zone of radius r_0. For a homogeneously contracting network, the divergence of the velocity field will be constant and equal to the volume contraction rate, c, so that, $div(V) = \frac{1}{r^2}\frac{\partial}{\partial r}\left(r^2 V\right) = -c$ and $V(r_0) = 0$. The velocity profile in this case will be $V(r) = -\frac{c}{3} r\left(1 - \frac{r_0^{\ 3}}{r^3}\right)$. For $r_0 = 0$, we obtain a linear velocity profile $V(r) = -kr$ with $k = \frac{c}{3}$. For $r_0 > 0$, the velocity profile has a non-linear correction and the slope of the velocity profile is equal to $\frac{dV}{dr} = -\frac{c}{3}\left(1 + 2\frac{r_0^{\ 3}}{r^3}\right)$, so the magnitude of the slope increases as r approaches r_0.

In our experiments, r_0 ranges between 5-13 µm, with a mean value of r_0=8 µm (Fig. S1). For a homogeneously contracting network with r_0=8 µm, the non-linear correction term which scales like $\frac{r_0^3}{r^3}$ will shift the magnitude of the slope of a linear fit to the velocity profile in the range considered ($5\mu m < r - r_0 < 30\mu m$) by ~10%. The determination of the contraction rate from the slope of the experimental velocity profiles ignores this correction, which is comparable to the typical droplet-to-droplet variation in our data. Alternatively, we can calculate the volume contraction rate directly from the data assuming spherical symmetry by computing $-div(V) = -\frac{1}{r^2}\frac{\partial}{\partial r}\left(r^2 V\right)$ (as in Figs. 3d, S3e).

We note that for values of r close to r_0, the experimentally measured velocity profiles differ from the velocity profile of a homogeneously contracting network. Specifically, the magnitude of the slope of the experimental velocity profiles close to r_0 decreases, indicating that the rate of network contraction decreases near the inner boundary. In these regions, where network density is high and network flow is slow, our assumption that the viscous stress dominates no longer holds and the elastic component of the stress likely slows down contraction.

The network density distribution

We consider a steady-state, spherically-symmetric network with a radial flow velocity field $V(r)$, a density $\rho(r)$, and an inner exclusion zone of radius r_0. We assume that the network turns over with constant actin assembly and disassembly rates equal to α and β, respectively, so the divergence of the network flux is equal to $\nabla \cdot \vec{J}(r) = \alpha - \beta\rho(r)$. For the spherically-symmetric case, the divergence of the flux is given by,

$$\nabla \cdot \vec{J}(r) = \frac{1}{r^2}\frac{\partial(r^2 V\rho)}{\partial r} = \rho\frac{1}{r^2}\frac{\partial(r^2 V)}{\partial r} + V\frac{\partial\rho}{\partial r} = \rho\,\nabla\cdot\vec{V} + V\frac{\partial\rho}{\partial r}.$$

Thus, for a given network velocity profile, $V(r)$, the network density distribution, $\rho(r)$, will be the solution of the following equation,

$$\frac{\partial \rho}{\partial r} = \frac{1}{V}\left[\alpha - \left(\beta + \nabla \cdot \vec{V}\right)\rho\right].$$

If we take a linear velocity profile, $V = -k\left(r - r_0\right)$, with a constant slope *k*, we obtain:

$$\frac{\partial \rho}{\partial r} = \frac{1}{-k\left(r - r_0\right)}\left[\alpha - \left(\beta - 3k + \frac{2kr_0}{r}\right)\rho\right].$$

For a given r_0, the network density profile depends only on the ratio between the contraction rate, *k*, and the turnover rate, β:

$$\frac{\partial \rho_0}{\partial r} = \frac{-1}{\left(r - r_0\right)}\left[1 - \left(\frac{\beta}{k} - 3 + \frac{2r_0}{r}\right)\rho_0\right] \qquad \rho = \frac{\alpha}{k}\rho_0 .$$

The density distribution is obtained by solving this equation, with a boundary condition that the network density vanishes at the droplet boundary $\rho_0\left(R_{drop}\right) = 0$. To obtain an explicit analytic solution we take $R_{drop} = 5r_0$ which approximates our experimental conditions (see Fig. S1f). The analytic solution for the density distribution as a function of position is plotted for the measured values of the turnover and contraction rates from our data, $\langle\beta\rangle = 1.4\,\mathrm{min}^{-1}$ and $\langle k\rangle = 0.65\,\mathrm{min}^{-1}$ respectively, and nicely matches the measured density distribution (Fig. 4c).

This analysis indicates that for a given r_0, the normalized network density profile depends only on the ratio between the turnover rate and the contraction rate. Thus, when the turnover rate and the contraction rate increase, but their ratio remains constant, the large-scale network density profile remains unchanged, but the network dynamics (both flow and turnover) become faster. For different values of β/k, we characterize the spatial extent of the network density by the distance between the inner boundary (r_0) and the position where the network reaches its half-maximal value ($R_{1/2}$). To account for differences in droplet sizes, we define a relative network width as $\frac{R_{1/2} - r_0}{R_{drop} - r_0}$. Figure 4d shows that the predicted relative network width increases as a function of β/k. The dependence of the network density profile and dynamics as a function of the turnover and contraction rates from this model are summarized schematically in Fig. 4g.

The density distribution determined from this simple model which assumes constant turnover and contraction rates characterized by β and k, respectively, compares well with the measured density distributions for different conditions (Fig. 4c,d). In particular, the theoretical analysis nicely captures the changes in the spatial extent of the network as the ratio between the turnover rate and the contraction rate varies, leading to markedly more extended networks with added ActA and more condensed networks with added α-Actinin (Fig. 4d). Note that the turnover rate and/or the contraction rate can become density-dependent (as we observe e.g. following the addition of α-Actinin). In this case the local turnover and/or contraction rates will vary, and this will further influence the large-scale network density distribution.

Supplementary Figures

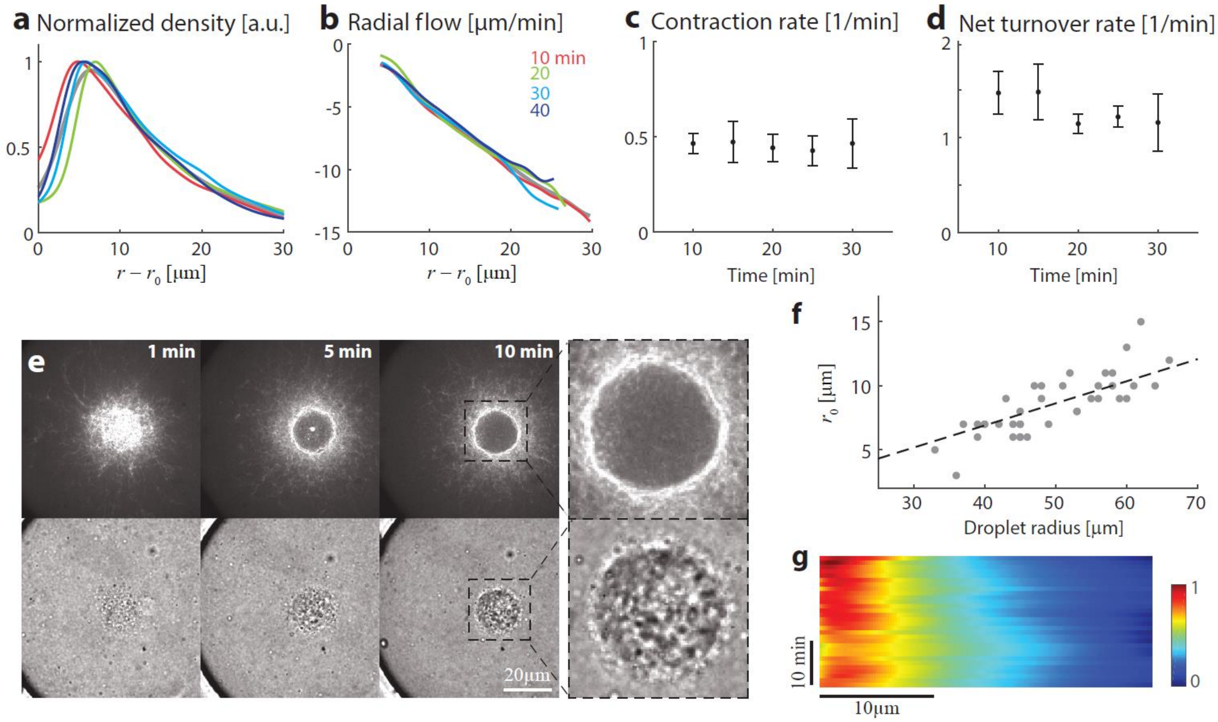

Figure S1. Steady-state dynamics in confined contractile actomyosin networks. (a-d) The network dynamics are measured in individual droplets labeled with GFP-Lifeact as a function of time, at 5 min time intervals. (a,b) The normalized actin network density (a) and radial velocity (b) are plotted as a function of distance from the contraction center for one droplet at different time points. (c,d) The contraction rate and net turnover rate in individual droplets are determined from the slopes of linear fits to the radial network flow as a function of distance, and the net turnover as a function of density, respectively. The average contraction (c) and turnover rates (d) are depicted as a function of time (mean ± std; N=6). The characteristics of the system remain nearly unchanged, indicating that the system is at steady-state. (e) Bright-field (bottom) and spinning disk confocal images (top) from a time-lapse movie of the equatorial cross section of a droplet showing the formation of the exclusion zone around the contraction center in the first minutes after sample preparation. After 10 min the exclusion zone stops growing and the system reaches a steady-state. (f) The radius of the exclusion zone in different droplets is plotted as a function of the radius of the droplet. The line depicts a linear fit to the data ($r_0 = 0.18R_{drop}$). (g) Kymograph showing the actin density over time in an individual droplet labeled with AlexaFluor488-conjugated actin. The droplet was imaged every minute. The background-corrected and bleach-corrected radial actin fluorescence signal (in a.u.) as a function of distance from the inner boundary (x-axis) is shown for different time points (y-axis). The actin density remains nearly unchanged, indicating that the system is at steady-state.

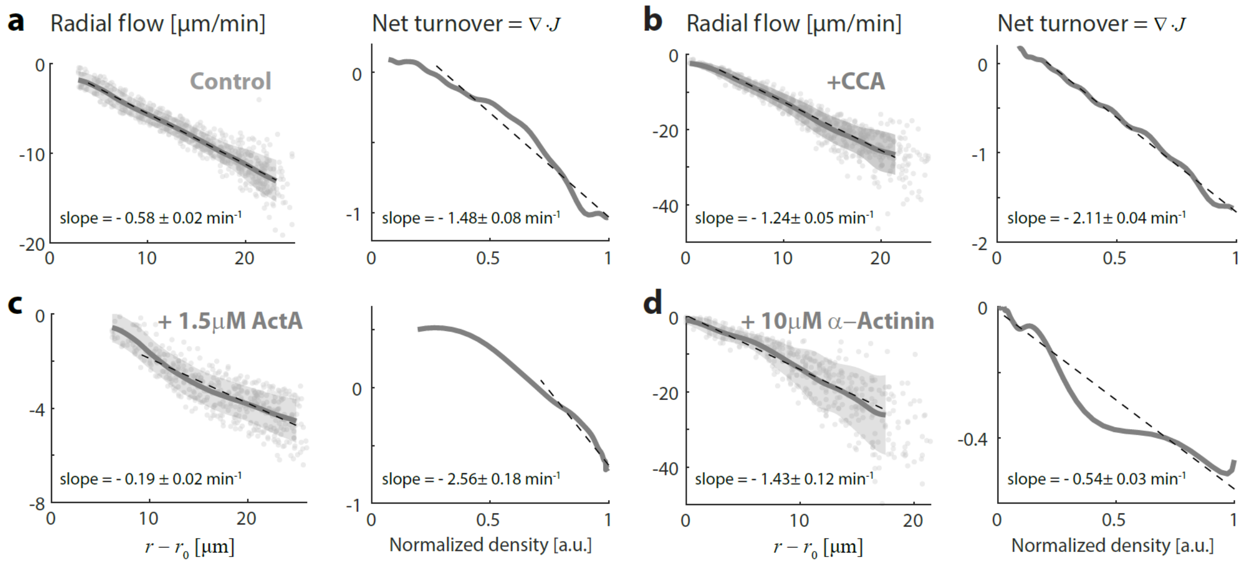

Figure S2. Results from individual droplets showing the raw data and the quality of the linear fits used to determine the contraction and turnover rates. (a-d) Left: the radial network flow rate is plotted as a function of distance from the contraction center for individual droplets. The velocity extracted from the correlation analysis at each grid point is depicted (dots; see Methods), together with the mean (line) and std (shaded region) radial velocity profile for each droplet. The linear fit (dashed line) to the velocity data (dots) is shown over the range used to determine the fit (see Methods). The contraction rate for each droplet was determined from the slope of this fit. The error in the contraction rate in individual droplets was estimated as the half-width of the 95% confidence interval for the slope as indicated on each graph. The mean error in the slope was < 6% (= 0.03 min^{-1} for the control samples; N=39). For all conditions, the maximal error in determining the slope at 95% confidence level in individual droplets was smaller than the variation between droplets (std = 0.15 min^{-1} for the control sample). Right: the net actin turnover as a function of network density is plotted for individual droplets. The average radial velocity and density profile for each droplet were used to calculate the divergence of the network flux which is equal to the net turnover (line). The linear fit to the net turnover as a function of density is shown over the range used to determine the fit (dashed line; see Methods). The turnover rate for each droplet was determined from the slope of this fit. The mean error in determining the slope in individual droplets was < 10% (=0.08 min^{-1} for the control samples), which is smaller than the variation between individual droplets (std=0.3 min^{-1} for the control sample). Data is shown for individual droplets with (a) 80% extract (control) and samples supplemented with (b) 12.5μM Cofilin, 1.3μM Coronin and 1.3 μM Aip1, (c) 1.5μM ActA, or (d) 10μM α-Actinin.

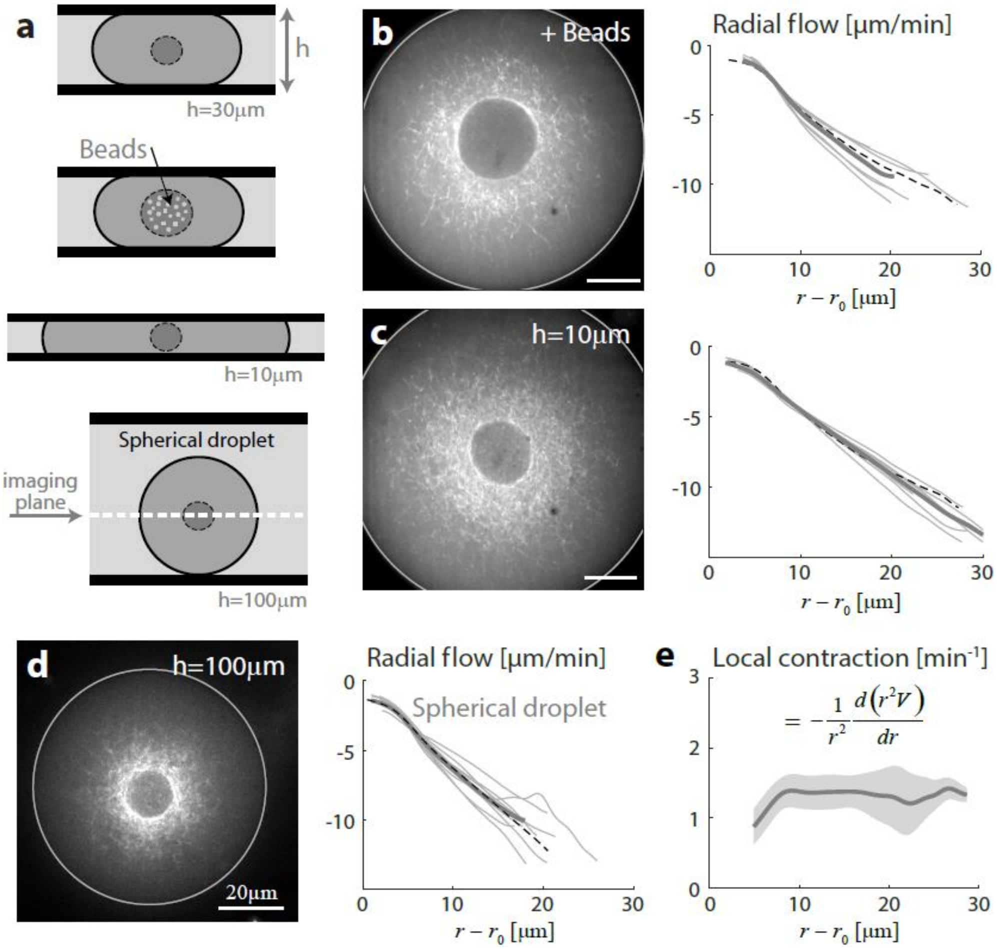

Figure S3. Network contraction does not depend on sample geometry. (a) Schematic illustrations of the different sample geometries used: squished droplets in a 30 μm-height chamber (standard geometry); (b) Squished droplet with added beads that increase the size of the inner exclusion zone, (c) Squished droplets in a 10 μm-height chamber, and (d) Spherical droplets (imaged in a 100 μm-thick chamber). In all cases the droplets were imaged at their equatorial plane. For (c) and (d) the samples were made normally, the only difference being the thickness of the sample chamber. For (b) the extract mix was supplemented with 1μm silica beads (which are pre-passivated by incubation with extract). The beads are swept inward by the contractile flow, and increase the diameter of the inner exclusion zone from ~20% of the droplets' diameter, to ~30% of the droplets' diameter. (b-d) For each geometry, a spinning disk confocal image of the equatorial cross section of the network labeled with GFP-Lifeact (left), is shown together with a graph of the radial network flow as a function of distance from the inner boundary (right). The thin grey lines depict data from individual droplets, and the thick lines depict the average over different droplets. The dashed lines show the results for the control sample in the standard geometry. In all cases, the radial velocity depends linearly on the distance from the inner boundary with the same slope, indicating that the networks exhibit homogeneous contraction with the same contraction rate, irrespective of the sample geometry. (e) For spherical droplets, the velocity field has spherical symmetry, so the local contraction rate is equal to $-\nabla \cdot V = -\frac{1}{r^2}\frac{d\left(r^2 V\right)}{dr}$. The contraction rate (mean and std; *N*=12) is plotted as a function of the distance from the inner boundary. The contraction rate is nearly constant for $r - r_0 > 10\mu m$.

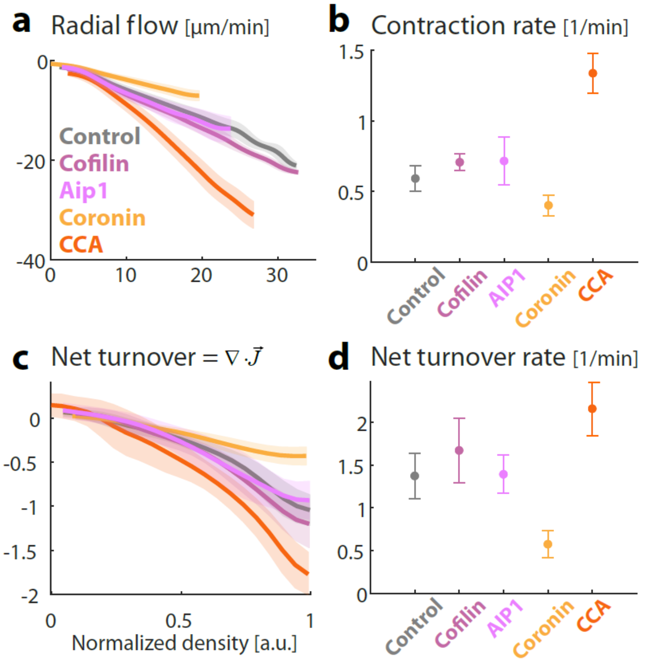

Figure S4. Networks dynamics with added components of the actin disassembly machinery, Cofilin, Coronin and Aip1. Contractile actin networks are generated by encapsulating *Xenopus* extract supplemented with either 12.5µM Cofilin (*N*=7), 1.3µM Coronin (*N*=8), 2.6 µM Aip1 (*N*=14) separately, or all three proteins together (CCA: 12.5µM Cofilin, 1.3 µM Coronin, and 1.3 µM Aip1; *N*=7). (a) The radial velocity is plotted as a function of distance from the inner boundary for the different conditions. For each condition, the mean (line) and std (shaded region) over different droplets are depicted. (b) The average contraction rate for each condition, determined from the slopes of linear fits to the radial velocity as a function of distance in individual droplets (as in Fig. S2; mean ± std). (c) The net actin turnover as a function of the normalized network density is plotted for the different conditions. For each condition, the mean (line) and std (shaded region) over different droplets are depicted. (d) The average net turnover rate for each condition, determined from the slopes of linear fits of the net turnover as a function of network density (as in Fig. S2; mean ± std). The net turnover rate and the contraction rate increase appreciably only when all three CCA proteins are added together. Addition of Coronin on its own, had an opposite effect. This may be due to Coronin's bundling activity [12], since similar effects are seen with the addition of the filament bundling protein Fascin (Fig. S6b).

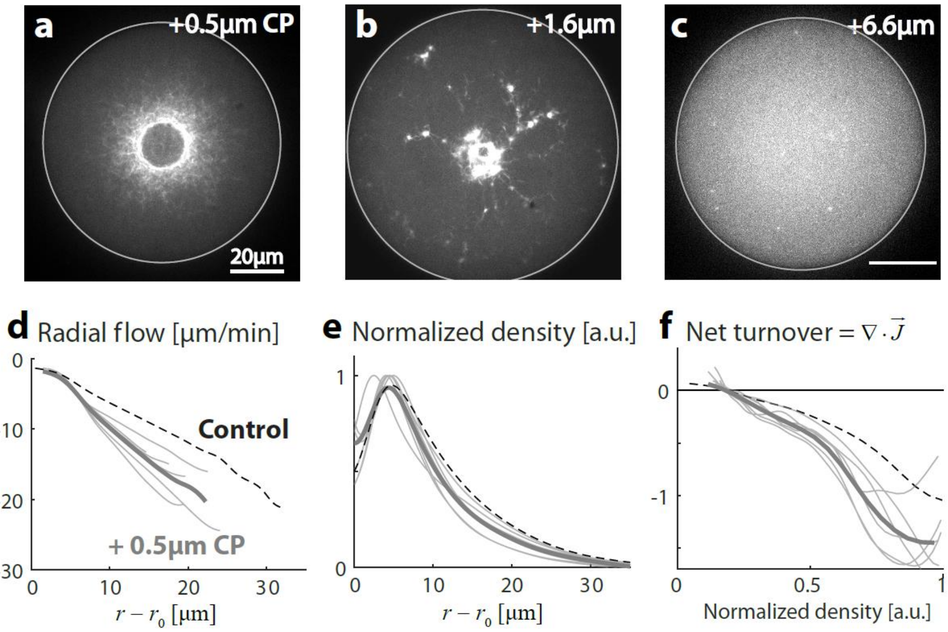

Figure S5. Networks dynamics with added Capping Protein. Contractile actin networks are generated by encapsulating *Xenopus* extract supplemented with different concentrations of Capping Protein (CP), which caps barbed ends and blocks actin assembly there. (a-c) Spinning disk confocal fluorescence images of the equatorial cross sections of networks labeled with GFP-Lifeact in samples supplemented with 0.5, 1.6 or 6.6µM CP, respectively. (a) At a concentration of 0.5µM CP, the system reaches a steady-state within minutes, with a density distribution similar to unsupplemented samples. (b) At a concentration of 1.6µM CP, the network is composed of loosely connected clusters that contract towards each other. (c) At even higher CP concentrations, network formation is entirely blocked due to excess capping activity, and the probe density becomes homogeneous. (d-e) The inward contractile flow and actin network density are measured for samples supplemented with 0.5µM CP. Graphs depicting the radial network flow (d) and density (e) as a function of distance from the inner boundary are shown. (f) Net actin turnover as a function of network density. The thin grey lines depict data from individual droplets, and the thick line is the average over different droplets. The dashed lines show the results for the control unsupplemented sample. Blocking assembly with CP leads to higher contraction rates and faster net turnover.

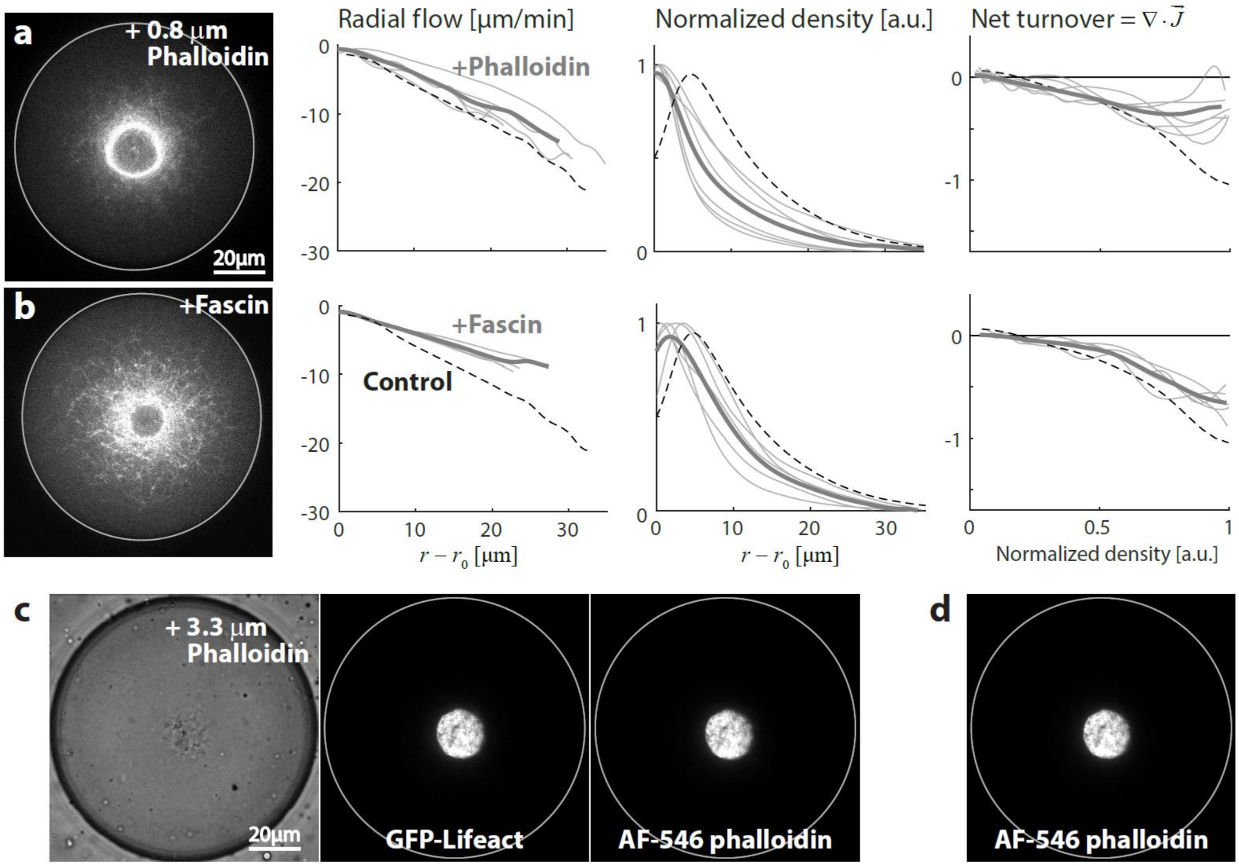

Figure S6. Network dynamics under additional perturbations. Contractile actin networks are generated by encapsulating *Xenopus* extract supplemented with (a) 0.8μM Phalloidin which reduces actin filament disassembly; or (b) 2.6μM Fascin which bundles actin filaments. In both cases, the system reaches a steady-state within minutes. The inward contractile flow and actin network density are measured (as in Figure 1). For each condition, a spinning disk confocal fluorescence image of the equatorial cross section of the network labeled with GFP-Lifeact (left) is shown, together with graphs depicting the steady-state radial network flow and density as a function of distance from the inner boundary (middle), and the net actin turnover as a function of network density (right). The thin grey lines depict data from individual droplets, and the thick line is the average over different droplets. The dashed lines show the results for the control unsupplemented sample. Stabilizing actin filaments with low levels of Phalloidin or adding the filament bundler Fascin leads to reduced turnover and slower contraction. (c,d) Adding higher concentrations of Phalloidin (3.3μM) inhibits actin turnover and completely abolishes the continuous network flows. Spinning disk confocal images of the equatorial cross section of a droplet containing 3.3 μM AlexaFluor 546-conjugated Phalloidin are shown ~10 min after sample preparation (c). In the presence of high concentrations of Phalloidin, the filaments aggregate at the center. Imaging the same droplet after 1min (d) illustrates that the aggregate at the center is not dynamic and there are no measurable actin networks flows.

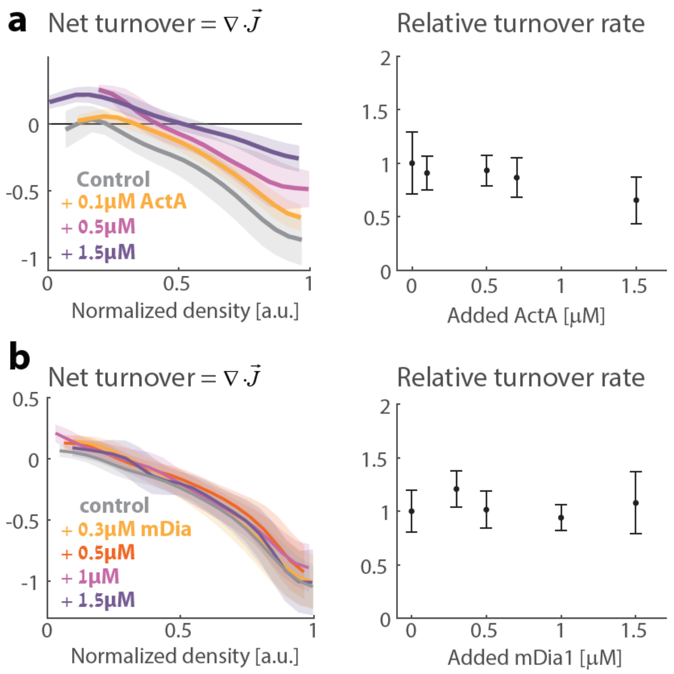

Figure S7. Net network turnover with added assembly promoting factors. Contractile actin networks are generated by encapsulating *Xenopus* extract supplemented with different concentrations of ActA (a) or mDia1 (b). The divergence of the network flux, which is equal to the net network turnover, is plotted as a function of the local normalized network density (left). The net turnover rate in individual droplets was determined from the slope of a linear fit to the divergence of the flux (net turnover) as a function of density. To obtain the relative turnover rates, these values were divided by the average net turnover rate for the unsupplemented control sample. The relative turnover rates averaged over different droplets for each condition (mean ± std) are plotted as a function of the added protein concentrations (right). The relative turnover rates are not statistically different from the control (0μM; p>0.01).

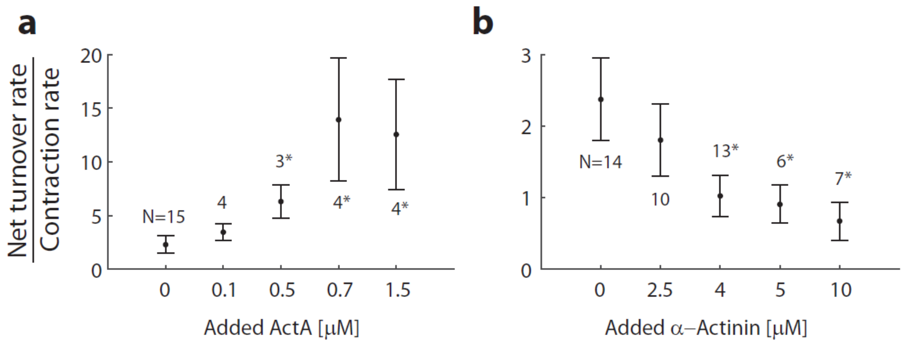

Figure S8. Changes in the ratio between the net turnover rate and the contraction rate with added ActA and α-Actinin. The net turnover rate and the contraction rate were determined for droplets made from samples supplemented with different concentrations of ActA (a) or α-Actinin (b) (as in Fig. S2). For each condition, the mean ± std values for the ratio between the net turnover rate and the contraction rate are shown. The number of droplets in each condition is indicated. The conditions that are statistically different from the control (0μM) are indicated (*, p<0.01).

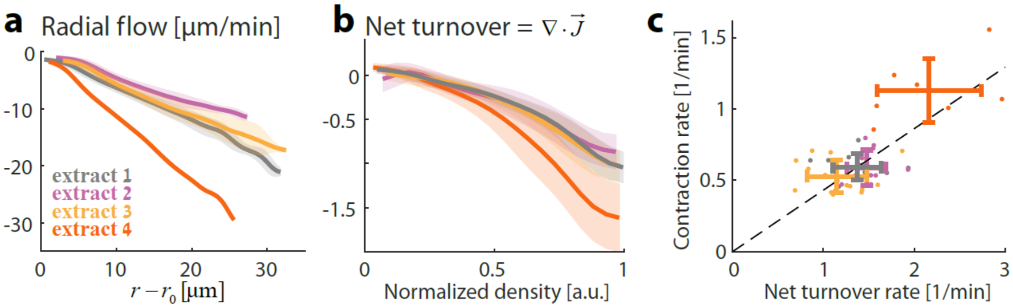

Figure S9. Network dynamics for different extract batches. Contractile actin networks are generated by encapsulating different batches of *Xenopus* extract. (a) The radial network flow rate is plotted as a function of distance from the inner boundary. (b) The net actin turnover as a function of network density is plotted. For each batch of extract, the mean (line) and std (shaded region) over different droplets are depicted. The extract denoted ‘extract 1’ (grey) is the one used for most of the comparative data presented. (c) A scatter plot of the contraction rate and net turnover rate for the different extract batches tested. For each extract, the dots depict values for individual droplets and the error bars show the mean and std of all the droplets examined for that extract. The dashed line indicates where the ratio between the contraction rate and turnover rate is equal to the ratio of the average values for ‘extract 1’.

Supplementary Movies:

Movie 1. Steady-state dynamics in a confined contracting actomyosin network. This movie shows spinning disc confocal images at the equatorial plane of a contracting actomyosin network labeled with GFP-Lifeact within a water-in-oil droplet. The field of view is 105μm wide, and the elapsed time is indicated.

Movie 2. Contracting actomyosin network supplemented with Cofilin, Coronin and Aip1. This movie shows spinning disc confocal images at the equatorial plane of a contracting actomyosin network labeled with GFP-Lifeact formed with extract supplemented with 12.5μM Cofilin, 1.3μM Coronin and 1.3μM Aip1. The field of view is 105μm wide, and the elapsed time is indicated.

Movie 3. Contracting actomyosin network supplemented with ActA. This movie shows spinning disc confocal images at the equatorial plane of a contracting actomyosin network labeled with GFP-Lifeact formed with extract supplemented with 0.75μM ActA. The field of view is 105μm wide, and the elapsed time is indicated.

Movie 4. Contracting actomyosin network supplemented with α–Actinin. This movie shows spinning disc confocal images at the equatorial plane of a contracting actomyosin network labeled with GFP-Lifeact formed with extract supplemented with 10μM α–Actinin. The field of view is 105μm wide and the elapsed time is indicated.

Supplementary References

1. Bausch, A.R., Ziemann, F., Boulbitch, A.A., Jacobson, K. & Sackmann, E. Local measurements of viscoelastic parameters of adherent cell surfaces by magnetic bead microrheometry. *Biophysical Journal* **75**, 2038-2049 (1998).
2. Keller, M., Tharmann, R., Dichtl, M.A., Bausch, A.R. & Sackmann, E. Slow filament dynamics and viscoelasticity in entangled and active actin networks. *Philosophical Transactions of the Royal Society of London A: Mathematical, Physical and Engineering Sciences* **361**, 699-712 (2003).
3. Kole, T.P., Tseng, Y., Jiang, I., Katz, J.L. & Wirtz, D. Intracellular mechanics of migrating fibroblasts. *Molecular Biology of the Cell* **16**, 328-338 (2005).
4. Wottawah, F. *et al.* Optical rheology of biological cells. *Physical Review Letters* **94**, 098103 (2005).
5. Panorchan, P., Lee, J.S.H., Kole, T.P., Tseng, Y. & Wirtz, D. Microrheology and ROCK signaling of human endothelial cells embedded in a 3D matrix. *Biophysical Journal* **91**, 3499-3507 (2006).
6. Rubinstein, B., Fournier, M.F., Jacobson, K., Verkhovsky, A.B. & Mogilner, A. Actin-myosin viscoelastic flow in the keratocyte lamellipod. *Biophysical Journal* **97**, 1853-1863 (2009).
7. Zhu, C. & Skalak, R. A continuum model of protrusion of pseudopod in leukocytes. *Biophysical journal* **54**, 1115-1137 (1988).
8. Jin, T., Li, L., Siow, R.C.M. & Liu, K.-K. A novel collagen gel-based measurement technique for quantitation of cell contraction force. *Journal of The Royal Society Interface* **12**, 20141365 (2015).
9. Yang, M.T., Reich, D.H. & Chen, C.S. Measurement and analysis of traction force dynamics in response to vasoactive agonists. *Integrative Biology* **3**, 663-674 (2011).
10. Yamada, S., Wirtz, D. & Kuo, S.C. Mechanics of living cells measured by laser tracking microrheology. *Biophysical Journal* **78**, 1736-1747 (2000).
11. Wuhr, M. *et al.* Deep proteomics of the Xenopus laevis egg using an mRNA-derived reference database. *Current Biology* **24**, 1467-1475 (2014).
12. Goode, B.L. *et al.* Coronin promotes the rapid assembly and cross-linking of actin filaments and may link the actin and microtubule cytoskeletons in yeast. *The Journal of cell biology* **144**, 83-98 (1999).